HHS Public Access

Author manuscript

J Chem Theory Comput. Author manuscript; available in PMC 2022 January 12.

Published in final edited form as:

J Chem Theory Comput. 2022 January 11; 18(1): 479–493. doi:10.1021/acs.jctc.1c00996.

CHARMM-GUI Nanomaterial Modeler for Modeling and Simulation of Nanomaterial Systems

Yeol Kyo Choi[1,†], **Nathan R. Kern**[1,†], **Seonghan Kim**[1,†], **Krishan Kanhaiya**[2], **Yaser Afshar**[3], **Sun Hee Jeon**[1], **Sunhwan Jo**[4], **Bernard R. Brooks**[5], **Jumin Lee**[1], **Ellad B. Tadmor**[3], **Hendrik Heinz**[2], **Wonpil Im**[1,*]

[1]Department of Biological Sciences, Chemistry, Bioengineering, and Computer Science and Engineering, Lehigh University, Bethlehem, PA 18015, USA

[2]Department of Chemical and Biological Engineering, University of Colorado at Boulder, Boulder, CO 80301, USA

[3]Department of Aerospace Engineering and Mechanics, University of Minnesota, Minneapolis, MN 55455, USA

[4]Leadership Computing Facility, Argonne National Laboratory, 9700 Cass Ave, Argonne, IL 60439, USA

[5]Laboratory of Computational Biology, National Heart, Lung and Blood Institute, National Institutes of Health, Bethesda, MD 20892, USA

Abstract

Molecular modeling and simulation are invaluable tools for nanoscience that predict mechanical, physicochemical, and thermodynamic properties of nanomaterials and provide molecular-level insight into underlying mechanisms. However, building nanomaterial-containing systems remains challenging due to the lack of reliable and integrated cyberinfrastructures. Here, we present *Nanomaterial Modeler* in CHARMM-GUI, a web-based cyberinfrastructure that provides an automated process to generate various nanomaterial models, associated topology, and configuration files to perform state-of-the-art molecular dynamics simulations using most simulation packages. The nanomaterial models are based on the interface force field (IFF), one of the most reliable FFs. The transferability of nanomaterial models among the simulation programs was assessed by single-point energy calculations, which yielded 0.01% relative absolute energy

*Corresponding author: wonpil@lehigh.edu.
†These authors contributed equally to this work.

SUPPORTING INFORMATION

Computational details S1–S7: detailed methods for simulation protocols of various simulation packages, nanomaterial model preparations, measurement of structural, mechanical, vibrational and thermodynamic properties, and preparations of complex nano-bio and nano-polymer systems; Table S1: simulation parameters for the nanomaterial simulations; Table S2: isothermal compressibility of nanomaterials; Table S3: single-point energy calculations of various simulation programs; Table S4 and S5: lattice parameters of supported nanomaterials; Table S6: computed densities of 18 fcc metals with three LJ cut-off methods; Figure S1: error estimation of computed densities of fcc metals with different LJ cut-off method; Figure S2: illustration of the solid-vapor surface energy calculation; Table S7: effect of LJ cut-off methods on the solid-vapor surface energy of fcc metals; Table S8 and Figure S3: computed densities of nanomaterials with three LJ cut-off methods; Figure S4: illustration of contact angle measurements of the silica surface; Figure S5: velocity autocorrelation function of α-cristobalite; Table S9: computed surface energies of nanomaterials with three LJ cut-off methods; Table S10: computed cleavage energies of hydroxyapatite in various pH conditions; Figure S6: illustration of Wulff construction of platinum.

differences for various surface models and equilibrium nanoparticle shapes. Three widely-used Lennard-Jones (LJ) cut-off methods are employed to evaluate the compatibility of nanomaterial models with respect to conventional biomolecular FFs: simple truncation at r = 12 Å (12 cut-off), force-based switching over 10 to 12 Å (10–12 fsw), and LJ particle mesh Ewald with no cut-off (LJPME). The FF parameters with these LJ cut-off methods are extensively validated by reproducing structural, interfacial, and mechanical properties. We find that the computed density and surface energies are in good agreement with reported experimental results, although the simulation results increase in the following order: 10–12 fsw < 12 cut-off < LJPME; nanomaterials in which LJ interactions are a major component show relatively higher deviations (up to 4% in density and 8% in surface energy differences) compared to the experiment. *Nanomaterial Modeler*'s capability is also demonstrated by generating complex systems of nanomaterial-biomolecule and nanomaterial-polymer interfaces with a combination of existing CHARMM-GUI modules. We hope that *Nanomaterial Modeler* can be used to carry out innovative nanomaterial modeling and simulation to acquire insight into the structure, dynamics, and underlying mechanisms of complex nanomaterial-containing systems.

Graphical Abstract

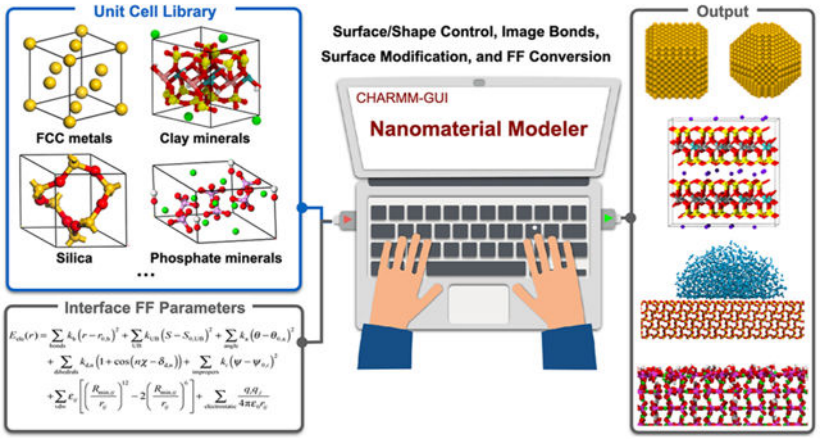

INTRODUCTION

Understanding the dynamical evolution of biological and materials systems at the atomic scale is essential for groundbreaking advances in health science, materials science, energy conversion, sustainability, and overall quality of life.[1–5] However, progress is limited as current experimental techniques alone cannot provide complete information about structures and dynamical processes at the nanometer to micrometer scale. Classical molecular modeling and simulation using force fields (FFs) and complex configuration databases are playing an increasingly important role in explaining experimental data, elucidating design principles, and making transformative property predictions for unknown biomolecular and nanomaterial structures and dynamics, as well as their interfaces. These computational methods are suitable for harnessing big data and accelerating discovery from the quantum scale to the microscale.[6–8]

State-of-the-art FFs for biomolecular systems (e.g., proteins, lipids, nucleic acids, and carbohydrates) have matured to the point where they can explain experiments and accelerate experimental discovery via testable hypotheses.[9, 10] The same is true for the growing number of surface models for nanomaterials and nanomaterial-biological (nano-bio) interfaces.[11, 12] In particular, the surface model database and parameters for metals, clay minerals, silica, apatites, layered materials (e.g., MoS_2 and graphite), cement minerals, and gas molecules in the INTERFACE force field[11] (IFF) routinely achieve more accurate predictions of surface energies, binding energies, and molecular recognition than typical density functional theory (DFT) methods and is compatible with biomolecular FFs.[13–15] These recent developments present a unique opportunity for the life and material sciences to harness the predictive power of computer simulation methods to explore a broad range of nano-bio interfaces and complex electrolytes.

A recent round-robin study showed that distinct user groups working with different simulation FFs and programs yielded inconsistent results even for calculating simple thermodynamic properties such as density and potential energy.[16] The lack of a reliable and unified cyberinfrastructure to build complex nano-bio interfaces poses major challenges to the molecular modeling and simulation community in terms of steep learning curves, risks of choosing unsuitable FF and faulty interface models, as well as mistakes in file conversion and input scripts that render simulations less useful or invalid. Several programs have been developed to help users to build nanomaterial model systems, including web applications, such as *NanoModeler*[17] and *PubVINAS*,[18] and stand-alone software packages such as *Atomic Simulation Environment (ASE)*,[19] *pysimm*,[20] *Molecular Simulation Design Framework (MoSDeF)*,[21] and *NanoMaterialCAD*.[22] *NanoModeler* supports 16 gold nanocluster models with ligand grafting function and *PubVINAS* provides 11 material types with corresponding physicochemical properties and/or bioactivities. *ASE*, *pysimm*, and *MoSDeF* provide methods to prepare various nanomaterial systems and API to integrate different features of existing software packages using Python-based scripting. *NanoMaterialsCAD* offers a graphical user interface (GUI) to build and manipulate a nanomaterial system. However, all aforementioned software requires significant preprocessing to prepare structures, topologies, and parameters of nanomaterials for simulation and/or is limited to use specific prebuilt nanostructures. Commercial packages also exist, such as *Material Studio*,[23] *Schrödinger*,[24] and *Amsterdam Modeling Suite*,[25] but, are not freely available to everyone. Furthermore, the models from these programs are not transferable to other molecular dynamics (MD) simulation packages. Therefore, building models of functional nano-bio materials such as nanoparticle therapeutics, imaging agents, biomineral structures, bioinspired composites, and biosensors has been challenging to accomplish. Moreover, the simulation input preparation for nanomaterials and nano-bio interfaces currently involves multiple operations by researchers. This process includes the choice of building tools or scripts and file conversion and reassignment of FF parameters depending on the chosen simulation platform. Unfortunately, no single, user-friendly cyberinfrastructure is available to accomplish these crucial tasks.

CHARMM-GUI (https://www.charmm-gui.org), a web-based GUI, provides a well-designed workflow to interactively construct various complex biomolecular systems and seamlessly handles complicated internal data structures and simulation input files for CHARMM,[26]

NAMD,[27] GROMACS,[28] AMBER,[29] GENESIS,[30] LAMMPS[31], TINKER,[32] Desmond,[33] and OpenMM[34] with several biomolecular FFs.[7] The simulation protocols are optimized[6] following the principles of the original FF development.[35, 36] Therefore, CHARMM-GUI is widely utilized in studies on the role of biomolecular motions, conformational changes, and thermodynamic relationships in biological function.

This work presents *Nanomaterials Modeler*, an important extension of CHARMM-GUI to a broad range of nanomaterials based on the IFF, which can bridge the gap between biomolecular and material simulations through compatibility with multiple simulation platforms.[8, 37] *Nanomaterial Modeler* enables researchers to build nanomaterials models with up to 5,000,000 atoms and addresses aforementioned needs by merging IFF and CHARMM-GUI in an easy-to-use and state-of-the-art platform. The following sections discuss the methods, workflow, available nanomaterials models, the user interface, supported simulation engines, validation of the models, and example applications. The paper ends with brief conclusions.

METHODS

1. Workflow of *Nanomaterial Modeler*

Currently, CHARMM-GUI *Nanomaterial Modeler* supports ten classes of nanomaterials, including fcc metals, clay minerals, calcium sulfates, cement minerals, calcium silicate hydrate, silica, phosphate minerals, transition metal dichalcogenides (TMDC), and carbonaceous materials (Table 1).

Figure 1A shows an overall nanomaterial system building process that has been generalized and automated in two subsequent steps. Each step is designed to incorporate a user's specific options through a web interface and run CHARMM input files. Individual input and output files, including the generated structure and an archive of all created files, are available at each step. Video demonstrations on how to use *Nanomaterial Modeler* are available on the CHARMM-GUI website (http://www.charmm-gui.org/demo/nanomaterial). *Nanomaterial Modeler* adopts a GUI that allows researchers to quickly check and design nanomaterials (i.e., size and shape of nanomaterials, chemical modification of the surface, and periodicity along each axis).

Step 1 - Building bulk crystal(s)—In step 1, users can set a material type, shape, Miller index, size, and periodicity along X, Y, and Z directions. A unit cell structure of a selected nanomaterial (Figure 1B) is used to generate a user-specified nanomaterial system through unit cell duplication and translation (Figure 1C).

Step 2 - Treatment of unbalanced atoms and surface modification—For specific nanomaterials, bonds between the primary and neighboring cells (i.e., image bonds) are required to model an infinite surface or molecule along with the periodic images. To facilitate such image bonds, the "patch information" necessary to create such connections has been defined for the currently supported nanomaterials (Figure 1D). The patch information includes all bonds, angles, dihedrals, and partial charge and atomic type information that are created when the primary cell connects to the 26 image cells. After

setting periodicity, *Nanomaterial Modeler* performs necessary surface ionization, defect generation, and/or surface chemical modification (Figure 1E). At the end, users can obtain a nanomaterial system with the desired structure, topology, FF parameters, and simulation configuration files for further simulation. Furthermore, the generated structure can be used in CHARMM-GUI *Multicomponent Assembler* to model nano-bio systems as described below.

Nanomaterial Modeler provides validated all-atom simulation inputs for various MD programs, including CHARMM, GROMACS, NAMD, LAMMPS, AMBER, GENESIS, and OpenMM, enabling researchers to employ the package of their choice (see Supporting Information, Table S1, and S2). In the original IFF, electrostatic interactions are calculated using the particle mesh Ewald (PME) method and two Lennard-Jones (LJ) potentials (i.e., the 12-6 and 9-6 forms) are adapted. *Nanomaterial Modeler* supports a 12-6 LJ potential since the conventional biomolecular FFs such as AMBER,[46] CHARMM,[47–49] GROMOS,[50] and OPLS-AA[51] have been developed with a 12-6 LJ potential:

$$V_{LJ}(r) = 4\varepsilon\left[(\sigma/r)^{12} - (\sigma/r)^{6}\right]$$

where r is the distance between two interacting particles, ε is the depth of the potential well, and σ represents the distance at which the particle-particle potential energy is zero. In practice, the V_{LJ} interactions are negligible at large distances, and therefore an energy cut-off is introduced at a certain interparticle distance. A 12 Å cutoff was chosen for IFF due to the rapid loss of electron-electron correlation of London dispersion interactions with distance after few layers of nearest neighbors in contrast to long-range Coulomb interactions between permanently charged atoms.[52, 53] Also, a 12 Å cut-off is generally accepted for various FFs. However, different cut-off methods are used in conventional biomolecular FFs for different FF forms. The most widely-used methods are: i) simple truncation at r = 12 Å (12 cut-off), ii) force-based switching over 10 to 12 Å (10–12 fsw[54]), and iii) LJ particle mesh Ewald (LJPME). To compare the implementations of all supported MD programs and LJ methods, single point energy calculations of hydroxyapatite and α-quartz were performed (Table S3). The results show that all simulation programs are in excellent agreement with a maximum difference of 0.01% in the total energy, indicating that the nanomaterials IFF is correctly implemented within CHARMM-GUI. Note that the small observed differences are inevitable due to the usage of slightly different conversion factors within the programs and 10–12 fsw function implemented in GROMACS are slightly different with other software.[55] In this work, the mechanical, physicochemical, and thermodynamic properties were analyzed using these LJ cut-off methods to assess the transferability of IFF for different simulation packages and ability to model complex nano-bio systems in combination with various biomolecular FFs.

2. Model building

The unit cell structures of all nanomaterials were obtained from X-ray diffraction data[56–58] and the interface force field (IFF) database[8]. Starting from the conventional unit cell, a series of lattice vector transformations are performed to create an ‘oriented’ unit cell (OUC) where the *a* and *b* lattice vectors are parallel to the plane with Miller indices (*hkl*).[59] Note that the

c lattice vector is not necessarily perpendicular to the plane, although an orthogonal vector obtained within a reasonable cell size is used. For example, 18 fcc metals with 13 Miller indices have $\alpha = \beta = \gamma = 90°$. All lattice parameters of OUC of supported nanomaterials are summarized in Table S4 and Table S5. Model building methods for larger models from multiple unit cells are described in Figure 1. All model building procedures are controlled by CHARMM scripts and individual input and output files, including the CHARMM scripts and an archive of all the created files (i.e., structure, topology, and configuration files), are available on the *Nanomaterial Modeler* (http://charmm-gui.org/input/nanomaterial). Details of complex nano-bio and nano-polymer system building are summarized in Supporting Information.

3. Computational details

All simulations used the interface force field (IFF) for nanomaterials, the CHARMM force field for proteins, peptides, and lipids, and the CHARMM generalized force field for polymer.[9, 36, 60] The TIP3P water model was utilized for water-containing systems. To achieve better sampling and check convergence, three independent molecular dynamics (MD) simulations were performed for each system. Periodic boundary conditions (PBCs) are employed for all simulations, and the particle mesh Ewald (PME) method[61] is used for long-range electrostatic interactions. A leap-frog algorithm was used to integrate Newton's equation of motion. The simulation time step is set to 1 fs for equilibration and 2 fs for the production run in conjunction with the SHAKE algorithm[62] to constrain the covalent bonds involving hydrogen atoms for all programs except GROMACS in which the LINCS algorithm[63] is used instead. All simulation trajectories were recorded every 10 ps except vibrational frequency calculation (see Supporting Information). For each nanomaterial model, all structure and corresponding parameter files are generated in the CHARMM format (i.e., rtf and prm files). For GROMACS, NAMD, and LAMMPS, *FF-Converter* in CHARMM-GUI[64] is used for format conversion from CHARMM data format to corresponding program readable formats. For specific nanomaterials, bonds between the primary and neighboring cells (image-bond) are required to model infinite surfaces or molecules along with the periodic images. *Nanomaterial Modeler* supports CHARMM, NAMD, GROMACS, LAMMPS, OpenMM, Amber, and Genesis for non-image-bond systems such as fcc metals. Four simulation programs, OpenMM, Gromacs, LAMMPS, and NAMD, are supported for image-bond systems. Three types of LJ cutoff methods, including 10–12 fsw, 12 cut-off, and LJPME are employed for the LJ interactions to investigate the cut-off method effect on the structural, physical, and mechanical properties. For LJPME, grid spacing and interpolation order were set to 1.2 Å and 4, respectively. Details of computational methods such as thermostat, barostat, and coupling constants for each simulation program are described in Supporting Information S1. Computational details of density, surface energies, mechanical properties, and vibrational spectra calculation for various nanomaterials are provided in Supporting Information S2–7. Details of computational methods, including density, surface energies, mechanical properties, and vibrational spectra, are provided in the Supporting Information.

RESULTS AND DISCUSSION

1. Metals: gold surfaces with various Miller indices and its equilibrium particle shapes

Nanomaterial Modeler supports 18 fcc metals (Table 1): Ac, Ag, Al, Au, Ca (α), Ce (γ), Cu, Es (β), Fe (γ), Ir, Ni, Pb, Pd, Pt, Rh, Sr (α), Th (α), and Yb (β). One can generate i) bulk crystal, ii) different cleavage surfaces with Miller indices ranging from (100) to (332) with any combination of periodicity, and iii) a variety of shapes such as a sphere, cylinder, rod, polygon, box, and Wulff construction. Figure 2A shows the user interface of *Nanomaterial Modeler* for building a (111) gold surface with a size of 51.9 × 59.9 × 35.3 $Å^3$; n.b., the input dimension and the final model dimension can be different because of the unit cell size. The selected (111) Miller index plane is perpendicular to the Z-axis. With user-specified X, Y, and Z dimensions, *Nanomaterial Modeler* displays an estimated system size from the unit cell information (see Supporting Information for lattice parameters of all unit cells). To build an infinite surface parallel to the XY plane with vacuum layers (i.e., a slab), periodicity can be selected in the X and Y directions and vacuum selected under “System Type”. This simple user interface enables easy system building for various fcc metals. With these options, a final all-atom model of (111) gold surface is illustrated in Figure 2B. In this work, experimental densities and surface energies are employed for model validation. Computed densities of 18 fcc metals with different LJ cut-off methods (i.e., 12 cut-off, 10–12 fsw, and LJPME) are in excellent agreement with the experimental data for all supported simulation programs (Table S6 and Figure S1). Solid-vapor interface tensions ($\gamma_{SV}^{(111)}$) for 18 fcc metals with 13 Miller indices were computed (Figure S2). Figure 2C shows comparison of computed and experimental $\gamma_{SV}^{(111)}$ of 18 fcc metals with three LJ cut-off methods. The 10–12 fsw, 12 cutoff, and LJPME reproduce surface energy for all fcc metals with less than −6.5%, 0.9%, and 6.5% deviations, respectively (Table S4 and S7).

Nanomaterial Modeler provides versatile methods to generate nanoparticle structures and surface modeling. One of the classic models to describe a particle shape is the Wulff construction[65] based on its orientation-dependent surface free energy. The computed surface energies of all fcc metals are presented in Table S4, which were used to generate the Wulff constructions (Figure 2D). One can select any combination of Miller indices and adjust surface energy values in the user interface. Figure 2D shows predicted equilibrium shapes using the Wulff construction and corresponding all-atom models of gold nanoparticles. Selecting (100) and (110) surfaces yield a cuboid (Shape 1). Changing from (110) to (111) produces a truncated octahedron (Shape 2). As the (100) surface energy increases, (100) surface area decreases and the shape changes to an octahedron (Shape 3). When a (110) surface is added to Shape 2, edges are covered with (110) surface and overall nanoparticle shape is closer to a spherical shape (Shape 4).

2. Clay minerals: Kaolinite, Pyrophyllite, Montmorillonite, and Muscovite

Clay minerals have been widely employed not only for industrial applications,[66] but also as additive biomaterials for drug delivery[67]. *Nanomaterial Modeler* provides facile modeling methods for four different clay minerals: kaolinite, pyrophyllite, montmorillonite, and muscovite. Unlike fcc metals, an infinite surface model of clay minerals has image bonds across the periodic boundary conditions (PBCs), and 27 image bonds are constructed. In

addition, some clay minerals may contain ions between layers, which can be measured by cation exchange capacity (CEC) states. For example, montmorillonite exists in various CEC states with different amounts of Mg replaced by Al. This substitution leaves net negative charges, which attracts cations for charge neutrality. *Nanomaterial Modeler* provides options to control the CEC states by randomly replacing Al with Mg and randomly distributing either Na^+ or K^+.

Figure 3A shows the user interface for building a montmorillonite surface model with 0.333 mmol/100g CEC, a size of 60 × 60 × 30 $Å^3$, and XY periodicity. Users can select desired CEC states by setting the ratio of the defect (i.e., a ratio of Al and Mg) and ion types. In addition, X and Y periodic options are selected to build an infinite surface along the XY plane. Representative snapshots of three clay minerals (pyrophyllite, montmorillonite, and muscovite) with various CEC states are shown in Figure 3B. The first row displays top views, where layers below the top layer are hidden for clarity. The second row illustrates a side view of each material. While pyrophyllite does not have ions in between layers, montmorillonite and muscovite do, and thus, the number of ions increases as the CEC states become larger. As a result, the spacing between layers of pyrophyllite is ~2.9 Å that is smaller than the other clay minerals due to the lack of ions between the layers (e.g., ~3.9 Å for montmorillonite and muscovite). Supported Miller indices and corresponding unit cell parameters are summarized in Table S5.

The densities, bulk modulus, and Young's modulus of the clay minerals are calculated with three different LJ cut-off methods to validate the model. Computed densities of clay minerals with other LJ cut-off methods show good agreement with experimental data with less than 4% deviation for all supported simulation programs (Table S8 and Figure S3). Figure 3C shows the bulk modulus of muscovite as a function of the applied pressure, which is in good agreement with a previously reported bulk modulus.[68] Also, all of the LJ cut-off methods yield consistent results; 10–12 fsw and LJPME have deviations of −2.6% and 3.7% relative to the 12 cut-off. In experiments, solid-vapor interface tensions (γ_{SV}) show a broad range from 0.050 to 0.200 J/m^2 because preparation process of Montmorillonite surface with specific CEC value is difficult, and even if the surface is made, the surface is very sensitive to environmental conditions such as humidity. The computed γ_{SV} of Montmorillonite are ranging from 0.087 to 0.113 J/m^2, which is consistent with the range observed in experiments (Table S9). For Muscovite, computed γ_{SV} reproduce experimental observation with less than 4 % deviation. Note that the energy differences of computed γ_{SV} among the LJ cut-off methods are negligible for all clay minerals.

Figure 3D represents Young's modulus of muscovite calculated along the Cartesian directions. The calculated moduli (132.0 GPa, 113.4 GPa, and 28.6 GPa for X, Y, and Z direction, respectively) show consistent trends and similar values to previous experimental and DFT results[69], although the values are about 10% lower. Identical to the reported study, the modulus along the X direction is approximately 16.4% larger than Y direction, and the modulus along the Z direction is smaller by at least 50% than either X or Y direction.

3. Silica: α-cristobalite silica slab with different surface chemistry

Silicon dioxide and silica are widely available in nature and biologically enriched in various organisms.[70, 71] These are also important materials in the semiconductor industry. The simulation of bulk and surface properties of silica has been of great interest since the emergence of computational modeling methods.[43, 72–74] *Nanomaterial Modeler* provides diverse modeling capabilities of silica that cover various surface chemistry and pH (i.e., the surface density of silanol and siloxide groups, and degree of ionization) for two shapes (box and sphere).

Figure 4A shows the user interface for building a surface of α-cristobalite with a 4.7 nm^{-2} density of silanol groups. The surface chemistry of silica depends on the surface characteristics (e.g., cleavage plane, particle size, and porosity), heat treatment, and environmental pH.[43] Various forms of silica at high pH contain Q^2 surface environments, which correspond to two silanol groups per superficial silicon atom ($=Si(OH)_2$), and mixed Q^2/Q^3 surface environments where Q^3 surface represents one silanol group per silicon atom ($\equiv Si(OH)$). The area density of silanol groups is in the range of 9.4 to 4.7 nm^{-2} (Figure 4B). Most silica glasses and medium size nanoparticles (~100 nm) contain 70–90% Q^3 environments on the surface (Figure 4C). The silica surfaces after thermal treatment consist of a high portion of Q^4 environments in which siloxide bridges without silanol groups (Figure 4D). All silanol groups on the silica surface are subject to deprotonation or/and protonation upon environmental conditions such as the area density of silanol groups, pH, ionic strength of the solution, and the type of ions present in solutions. In the physiological conditions with an ionic strength of 0.1~0.3 M of sodium ions, the ionization degree of silanol groups ranges from 0% to 20%. *Nanomaterial Modeler* supports ionization degrees up to 50% (Figure 4A). Figures 4E–G shows a Q^3 surface with a total Si-O(H,Na) density of 4.7 nm^{-2} with 5%, 15%, and 25% ionization, respectively.

The silica models show good agreement between computed and experimental properties of (1) densities, (2) water contact angles on the silica surfaces, (3) heat of immersion of silica surfaces in water, and (4) vibrational properties. Figure 5A shows the water contact angle, θ_c, on charge-neutral silica surfaces ranging from Q^3 to Q^4 environments in simulation and experiment.[75] The details of contact angle calculations are summarized in the Supporting Information and in Figure S4. The Q^3 surface exhibits a contact angle of $\theta_c = 0$. This surface is strongly hydrophilic due to the formation of hydrogen bonds between surface Si-OH groups and water molecules, thus fully wetted with water. Heat treatment from 200 to 1000°C decreases the area density of surface silanol groups due to condensation of adjacent silanol groups in Q^2 and Q^3 environments, yielding Q^4 environments. The transition in surface chemistry from Q^3 to Q^4 is modeled with 4.7, 2.35, 1.2, and 0 silanol groups per nm^2. Note that the silanol groups are non-ionized to represent interfaces with deionized water. The agreement between simulation and experimental measurements falls within ±3°. The heat of immersion (ΔH_{imm}) represents the enthalpy released upon immersion of clean particles or surfaces into the water and provides insight into silica-water interactions. Figure 5B shows a computational procedure to compute ΔH_{imm} of Q^3 silica surfaces in water. ΔH_{imm} of Q^3 silica obtained from calorimetric measurements is 160 ± 5 mJ/m^2 at 300 K, and the calculated results show good agreement within the uncertainty for all LJ cut-off

methods. The model also reproduces the vibrational frequency of silica with infrared and Raman measurements (Figure 5C and Figure S5). Strong bands at 960~1200 cm^{-1} and 600~800 cm^{-1} correspond to asymmetric and symmetric Si-O-Si stretching vibrations, respectively. The O-Si-O bending vibrations at 400~500 cm^{-1} and O-H stretching vibrations near 3700 cm^{-1} are also reproduced in the simulation. Although the computed value for one of the bands near 800 cm^{-1} is shifted approximately 100 cm^{-1} lower and the intensities of vibrational spectrum are not reproduced due to the lack of full electronic structure, most peak positions of the vibrational modes are clear and sufficient to monitor peak shifts in chemically different environments.

4. Phosphate minerals: hydroxyapatite with different surfaces and Wulff construction

Hydroxyapatite (HAP), $Ca_{10}(PO_4)_6(OH)_2$, is of great importance for human health because it is the major component in human bone and teeth and plays a central role in maladies such as osteoporosis.[44, 76] Atomistic models of HAP could facilitate a better understanding of the complex surface chemistry and provide insight into the interaction between biomolecules and HAP. Recent simulation results have shown that specific interactions between HAP surfaces and proteins are strongly dependent on pH, type of facet, surface defect, and specific details of the amino acid arrangement.[44, 77] To facilitate the research of HAP surface chemistry, surface models of various facets and nanocrystals as a function of pH are introduced in *Nanomaterial Modeler*.

Figure 6A shows the user interface for building a (001) HAP surface with a size of 60 × 60 × 30 $Å^3$ at pH ~10. *Nanomaterial Modeler* provides two shapes (box and Wulff construction). The number of possible (*hkl*) cleavage plane is in principle unlimited, but cleavage preferably occurs in (*hkl*) directions with weaker nonbonded interactions. *Nanomaterial Modeler* offers the common cleavage planes of HAP, (001), (010), (020), and (101), and surface models of HAP at various pH conditions, including pH ~5, ~10, and > 14 (see details in Supporting Information). MD simulations were performed to investigate the cleavage energies of the common low index planes of HAP (Figure 6B). The computed cleavage energies of PO_4^{3-} terminated surfaces range from 897.0 to 1223.3 mJ/m^2 and increase in the following order: (001) < (101) < (010) < (020). Note that the cleavage energy differences among the simulation packages are negligible (Table S9). For the LJ cut-off methods, 10–12 fsw and LJPME produce only −2.4% and 3.2% deviations relative to the 12 cut-off method (Table S10). Such a small difference compared to the deviations observed for fcc metals arises from the fact that electrostatic interactions dominate the HAP surface energy (see details in Supporting Information). In an experiment, the preparation of ideal cleaved surfaces of HAP is complex as they are hygroscopic and thus sensitive to environmental conditions such as humidity. To our knowledge, direct measurements of cleavage energies in vacuum have not been reported. Nevertheless, the cleavage energies of minerals with similar chemical composition and previously calculated cleavage energies for HAP are in good agreement with the current simulation results (see Table S10).

Nanomaterial Modeler enables modeling of HAP nanocrystals (i.e., Wulff construction) and various surface models. Figure 6C illustrates predicted shapes of HAP nanocrystal and final all-atom models according to the combination of Miller indices and corresponding surface

energies. Like the Wulff construction of gold nanoparticles in Figure 2, one can freely change the surface energy values in the text box and add/delete surfaces by clicking the ± button. In addition, the environment pH option can be specified during Wulff construction. Since cleavage energies are highly affected by environment pH, *Nanomaterial Modeler* automatically updates energy values and predicts corresponding shapes based on the selected pH range.

5. Transition Metal Dichalcogenide: MoS_2

Two-dimensional (2D) materials, including graphene and transition metal dichalcogenides (TMDC), such as molybdenum disulfide (MoS_2), have received significant attention due to their unique structural and electronic properties.[78, 79] *Nanomaterial Modeler* provides a facile modeling capability for graphene and 2H-MoS_2.

Figure 7A shows the user interface for building four 2H-MoS_2 layers with a size of 50 × 50 × 24 $Å^3$. In the Unit Cell Info section, one can set the number of MoS_2 layers to be generated according to the Z-length value in the Box Options. Note that MoS_2 is limited to XY-PBC as there is no information available for surface-end modification. The cleavage energy of the basal plane of a layered material is a key property for its applications. To evaluate the cleavage energy of MoS_2, a potential energy difference of two systems (i.e., a box of surface slab separated with a 60 Å vacuum layer (E_{sep}) and an equivalent periodic bulk model of the same number of atoms without a vacuum layer (E_{bulk})) is computed with 10–12 fsw, 12 cut-off, and LJPME using four simulation packages (Figure 7B and Supporting Information). The results agree with an experimental observation of 150 ± 10 mJ/m^2 for 12 cut-off. The use of different cut-off methods yields 137 ± 2 mJ/m^2 (10–12 fsw) and 156 ± 1 mJ/m^2 (LJPME), respectively. These relatively high deviations are also observed in the fcc metal cases as LJ interactions are the major component for their cleavage energy. For MoS_2, the contributions of LJ and electrostatic interactions to the cleavage energy are 93% and 7%, respectively. This indicates that, when LJ interaction is the main contributing factor to the cleavage energy, the LJ parameter adjustments for 10–12 fsw and LJPME methods are required to achieve the level of accuracy at experiment.

Structural and mechanical properties, as well as surface properties are essential factors to validate the MoS_2 model.[15] Figure 7C shows that the computed XRD pattern from experiment and simulation. The characteristic peak of MoS_2 is observed at 14.4°, corresponding to the (002) plane, and agrees well with experimental observation. For mechanical properties, the compressibility is computed with 12 cut-off method by recording the volume change at different pressures (1, 2, 3, and 4 GPa) and compared to the experiment (Figure 7D). The simulation results are identical with experiment up to about 2 GPa. Even when the pressure exceeds 2 GPa, the difference between the computed and experimental data remain below a 2% deviation.

6. Complex system

Several complex nano-bio systems are modeled and simulated to illustrate the potential use of *Nanomaterial Modeler* in combination with other CHARMM-GUI modules. Note that these illustrative systems are chosen to show the new capability of *Nanomaterial*

Modeler but not for FF validation. As a first example, a platinum (Pt) nanoparticle system with T7 peptides (acyl-TLTTLTN-amide) is built using three modules in CHARMM-GUI: *Nanomaterial Modeler* for the Pt nanoparticle, *PDB Reader & Manipulator*[7, 80] for T7 peptides, and *Multicomponent Assembler* for assembly of all models and solvation (Figure 8A). A cuboctahedron Pt nanoparticle is generated using Wulff construction (Shape 2 in Figure 2 and Figure S6) and located at the system center. T7 peptides are randomly distributed in the system with 3, 6, 12, 18, and 36 peptides corresponding to concentrations of 5, 10, 20, 50, and 100 μg/ml (see Methods and Supporting Information for details of the system building and simulation methods). After MD simulations of 200 ns duration, all T7 peptides are adsorbed onto the nanoparticle surface at all concentration levels (Figure 8B). At low concentration (< 20 μg/ml), the binding of the T7 peptides to the Pt nanoparticle occurred preferentially near edges as opposed to the inner portions of the (100) facets. This is due to the substantially reduced binding of water at the edges, which is consistent with previously reported data.[81] These simulations provide insight into the mechanisms of nanocrystal growth and the spatial distribution of facet-specific ligands as a function of concentration.

As a second example, 10th type III modules of fibronectin (FN-III10, PDB ID: 1TTF[82]) on a HAP surface are generated (Figure 8C). Fibronectin (FN) is known to regulate cell adhesion, growth, differentiation, or survival of osteoblasts, and support osteogenic cell responses in vitro.[83] This complex nano-bio interface system can be readily generated using a combination of the *Nanomaterial Modeler*, *PDB Reader*, and *Multicomponent Assembler* modules. This system can be used to investigate the effects of HAP surface properties on the adsorption of FN modules, which is important because the surface topology may modulate the biological activity of FN and the corresponding cell adhesion process.

The third example consists of a supported lipid bilayer (SLB) that is a popular model of cell membranes with potential biotechnological applications.[84] Many experimental techniques such as atomic force microscopy (AFM), quartz crystal microbalance with dissipation monitoring (QCM-D), and ellipsometry have been employed to investigate the structure and physical properties of lipid bilayers reconstituted with membrane proteins.[85, 86] However, most of these methods only provide superficial information and/or lack molecular-level insight into underlying mechanisms. Figure 8D shows an SLB system built using a combination of the *Nanomaterial Modeler*, *Membrane Builder*,[87–89] and *Multicomponent Assembler* modules (see Methods and Supporting Information).

In addition to various nano-bio interfaces, *Nanomaterial Modeler* can also be used to build polymer-containing nanomaterial systems (i.e., nano-polymers). As a final example, a nano-polymer complex system that consists of a cement mineral (in this case, tobermorite) and poly(acrylic acid) (PAA) was investigated. It is known that PAA strongly binds to the cement surface via ionic or possibly chelate binding and induces the cement to harden. Three modules in CHARMM-GUI are employed: *Nanomaterial Modeler* for tobermorite, *Polymer Builder*[60] for PAA, and *Multicomponent Assembler* for integration and solvation. A tobermorite (004) slab is located in the simulation box, and a 60% ionized PAA chain is placed 10 Å above the surface (Figure 8E). At an early simulation stage, carboxylates in the

PAA side chains begin to interact with the surface via strong ionic bonds with Ca^{2+} ions, and finally, the entire polymer chain is adsorbed on the surface.

CONCLUSIONS

This work presents *Nanomaterial Modeler* in CHARMM-GUI, a web-based cyberinfrastructure for building all-atom models of various nanomaterials and providing all necessary FF and configurational files for MD simulations. The model building workflow is generalized and automated in two steps: (i) building a bulk crystal through duplication and translation of a unit cell structure, and (ii) applying image patches and capping unbalanced atoms based on periodicity and chemical environment. *Nanomaterial Modeler's* versatile and efficient modeling features are illustrated by building various nanomaterial surface models and equilibrium nanoparticle shapes. Moreover, the transferability of nanomaterial models among the simulation programs was assessed by single-point energy calculations, which yielded 0.01% relative absolute energy differences for various surface models and equilibrium nanoparticle shapes. The significance of this work is that *Nanomaterial Modeler* provides a convenient modeling capability for various nanomaterial systems. Generated nanomaterial models can be used to model complex systems with other CHARMM-GUI modules, as demonstrated here with selected representative test cases.

To assess the transferability of our models and the IFF, we have investigated the effect of LJ cutoff methods on the structural, mechanical, and thermodynamic properties of nanomaterials. We have determined that the different LJ cut-off methods exhibit overall consistent results for most nanomaterial cases. The exceptions are nanomaterials for which LJ interactions are a major component for their cleavage energy. Such systems exhibit relatively larger deviations (up to 8%) compared to the electrostatic-driven materials if an LJ cut-off other than 12 Å is used. However, in most cases deviations are minor and consistent cut-offs or adjustments in the ε and σ parameters can be explored. Future work will include testing transferability for other nanomaterial properties and comparison with reactive and machine learning FFs through the OpenKIM framework.[90] We hope that *Nanomaterial Modeler* can be useful for carrying out innovative and novel nanomaterial modeling and simulation research to acquire insight into structures, dynamics, and underlying mechanisms of complex nano-bio and nano-polymer interface systems.

Supplementary Material

Refer to Web version on PubMed Central for supplementary material.

ACKNOWLEDGMENT

This work was supported in part by grants from NIH GM138472 (WI), NSF OAC-1931343 (WI), NSF OAC-1931587 (HH), and NSF OAC-1931304 (EBT).

DATA AVAILABILITY

Nanomaterial Modeler can be accessed through the following link: https://www.charmm-gui.org/input/nanomaterial. Under "References for Nanomaterial Modeler:" in the front

page of *Nanomaterial Modeler*, one can also obtains initial coordinates, topology, and configuration files of five representative systems, which include 1) surface tension of Au {111} surface, 2) surface energy of Muscovite, 3) contact angle measurement of silica surfaces, 4) Pt nanoparticle with T7 peptides, and 5) supported lipid bilayer system. Detailed procedures on how to build nanomaterial models using *Nanomaterial Modeler* are described in video demonstration (https://www.charmm-gui.org/demo/nanomaterial). Tutorial 1: overview of *Nanomaterial Modeler*; Tutorial 2: surface model and Wulff construction of fcc metal; Tutorial 3: building clay mineral models; Tutorial 4: Building calcium sulfate models; Tutorial 5: building cement mineral models; Tutorial 6: modeling nanoparticle and surfaces of silica; Tutorial 7: modeling nanocrystal and surfaces of hydroxyapatite; Tutorial 8: modeling molybdenum disulfide; Tutorial 9: modeling carbon nanotube and graphene. Questions related to the performance of IFF for the nanomaterials and related simulation settings can be directed to HH (hendrik.heinz@colorado.edu).

REFERENCES

(1). Yang Y; Chen CC; Scott MC; Ophus C; Xu R; Pryor A; Wu L; Sun F; Theis W; Zhou J; Eisenbach M; Kent PR; Sabirianov RF; Zeng H; Ercius P; Miao J, Deciphering chemical order/disorder and material properties at the single-atom level. Nature 2017, 542, 75–79. [PubMed: 28150758]

(2). Yeom B; Sain T; Lacevic N; Bukharina D; Cha SH; Waas AM; Arruda EM; Kotov NA, Abiotic tooth enamel. Nature 2017, 543, 95–98. [PubMed: 28252079]

(3). Chen J; Zhu E; Liu J; Zhang S; Lin Z; Duan X; Heinz H; Huang Y; De Yoreo JJ, Building two-dimensional materials one row at a time: Avoiding the nucleation barrier. Science 2018, 362, 1135–1139. [PubMed: 30523105]

(4). Heinz H; Pramanik C; Heinz O; Ding Y; Mishra RK; Marchon D; Flatt RJ; Estrela-Lopis I; Llop J; Moya S; Ziolo RF, Nanoparticle decoration with surfactants: Molecular interactions, assembly, and applications. Surf. Sci. Rep 2017, 72, 1–58.

(5). Bai Y; Zhang R; Ye X; Zhu Z; Xie H; Shen B; Cai D; Liu B; Zhang C; Jia Z; Zhang S; Li X; Wei F, Carbon nanotube bundles with tensile strength over 80 GPa. Nat. Nanotechnol 2018, 13, 589–595. [PubMed: 29760522]

(6). Lee J; Cheng X; Swails JM; Yeom MS; Eastman PK; Lemkul JA; Wei S; Buckner J; Jeong JC; Qi Y; Jo S; Pande VS; Case DA; Brooks CL 3rd; MacKerell AD Jr.; Klauda JB; Im W, CHARMM-GUI Input Generator for NAMD, GROMACS, AMBER, OpenMM, and CHARMM/OpenMM Simulations Using the CHARMM36 Additive Force Field. J. Chem. Theory Comput 2016, 12, 405–13. [PubMed: 26631602]

(7). Jo S; Kim T; Iyer VG; Im W, CHARMM-GUI: a web-based graphical user interface for CHARMM. J. Comput. Chem 2008, 29, 1859–65. [PubMed: 18351591]

(8). Heinz H; Lin T-J; Kishore Mishra R; Emami FS, Thermodynamically consistent force fields for the assembly of inorganic, organic, and biological nanostructures: the INTERFACE force field. Langmuir 2013, 29, 1754–1765. [PubMed: 23276161]

(9). Huang J; MacKerell AD Jr., CHARMM36 all-atom additive protein force field: validation based on comparison to NMR data. J. Comput. Chem 2013, 34, 2135–45. [PubMed: 23832629]

(10). Wang J; Wolf RM; Caldwell JW; Kollman PA; Case DA, Development and testing of a general amber force field. J. Comput. Chem 2004, 25, 1157–74. [PubMed: 15116359]

(11). Heinz H; Lin TJ; Mishra RK; Emami FS, Thermodynamically consistent force fields for the assembly of inorganic, organic, and biological nanostructures: the INTERFACE force field. Langmuir 2013, 29, 1754–65. [PubMed: 23276161]

(12). Heinz H; Ramezani-Dakhel H, Simulations of inorganic-bioorganic interfaces to discover new materials: insights, comparisons to experiment, challenges, and opportunities. Chem. Soc. Rev 2016, 45, 412–48. [PubMed: 26750724]

(13). Mishra RK; Kanhaiya K; Winetrout JJ; Flatt RJ; Heinz H, Force field for calcium sulfate minerals to predict structural, hydration, and interfacial properties. Cem. Concr. Res 2021, 139.

(14). Mark LO; Zhu C; Medlin JW; Heinz H, Understanding the Surface Reactivity of Ligand-Protected Metal Nanoparticles for Biomass Upgrading. ACS Catalysis 2020, 10, 5462–5474.

(15). Liu J; Zeng J; Zhu C; Miao J; Huang Y; Heinz H, Interpretable molecular models for molybdenum disulfide and insight into selective peptide recognition. Chem. Sci 2020, 11, 8708–8722. [PubMed: 34094188]

(16). Schappals M; Mecklenfeld A; Kröger L; Botan V; Köster A; Stephan S; García EJ; Rutkai G; Raabe G; Klein P, Round robin study: Molecular simulation of thermodynamic properties from models with internal degrees of freedom. J. Chem. Theory Comput 2017, 13, 4270–4280. [PubMed: 28738147]

(17). Franco-Ulloa S; Riccardi L; Rimembrana F; Pini M; De Vivo M, NanoModeler: A Webserver for Molecular Simulations and Engineering of Nanoparticles. J. Chem. Theory Comput 2019, 15, 2022–2032. [PubMed: 30758952]

(18). Yan X; Sedykh A; Wang W; Yan B; Zhu H, Construction of a web-based nanomaterial database by big data curation and modeling friendly nanostructure annotations. Nat. Commun 2020, 11, 2519. [PubMed: 32433469]

(19). Larsen AH; Mortensen JJ; Blomqvist J; Castelli IE; Christensen R; Dułak M; Friis J; Groves MN; Hammer B; Hargus C, The atomic simulation environment—a Python library for working with atoms. J. Phys.: Condens. Matter 2017, 29, 273002. [PubMed: 28323250]

(20). Fortunato ME; Colina CM, pysimm: A python package for simulation of molecular systems. SoftwareX 2017, 6, 7–12.

(21). Summers AZ; Gilmer JB; Iacovella CR; Cummings PT; McCabe C, MoSDeF, a python framework enabling large-scale computational screening of soft matter: Application to chemistry-property relationships in lubricating monolayer films. J. Chem. Theory Comput 2020, 16, 1779–1793. [PubMed: 32004433]

(22). Nikoulis G; Grammatikopoulos P; Steinhauer S; Kioseoglou J, NanoMaterialsCAD: Flexible Software for the Design of Nanostructures. Adv. Theory Simul 2020, 4.

(23). BIOVIA, Dassault Systèmes, Material Studio, San Diego: Dassault Systèmes, 2020.

(24). Schrödinger Release 2021–2: Maestro, Schrödinger, LLC, New York, NY, 2021.

(25). te Velde G; Bickelhaupt FM; Baerends EJ; Fonseca Guerra C; van Gisbergen SJA; Snijders JG; Ziegler T, Chemistry with ADF. J. Comput. Chem 2001, 22, 931–967.

(26). Brooks BR; Brooks CL 3rd; Mackerell AD Jr.; Nilsson L; Petrella RJ; Roux B; Won Y; Archontis G; Bartels C; Boresch S; Caflisch A; Caves L; Cui Q; Dinner AR; Feig M; Fischer S; Gao J; Hodoscek M; Im W; Kuczera K; Lazaridis T; Ma J; Ovchinnikov V; Paci E; Pastor RW; Post CB; Pu JZ; Schaefer M; Tidor B; Venable RM; Woodcock HL; Wu X; Yang W; York DM; Karplus M, CHARMM: the biomolecular simulation program. J. Comput. Chem 2009, 30, 1545–614. [PubMed: 19444816]

(27). Phillips JC; Braun R; Wang W; Gumbart J; Tajkhorshid E; Villa E; Chipot C; Skeel RD; Kale L; Schulten K, Scalable molecular dynamics with NAMD. J. Comput. Chem 2005, 26, 1781–802. [PubMed: 16222654]

(28). Abraham MJ; Murtola T; Schulz R; Páll S; Smith JC; Hess B; Lindahl E, GROMACS: High performance molecular simulations through multi-level parallelism from laptops to supercomputers. SoftwareX 2015, 1–2, 19–25.

(29). Case DA; Cheatham TE 3rd; Darden T; Gohlke H; Luo R; Merz KM Jr.; Onufriev A; Simmerling C; Wang B; Woods RJ, The Amber biomolecular simulation programs. J. Comput. Chem 2005, 26, 1668–88. [PubMed: 16200636]

(30). Jung J; Mori T; Kobayashi C; Matsunaga Y; Yoda T; Feig M; Sugita Y, GENESIS: a hybrid-parallel and multi-scale molecular dynamics simulator with enhanced sampling algorithms for biomolecular and cellular simulations. Wiley Interdiscip. Rev.: Comput. Mol. Sci 2015, 5, 310–323. [PubMed: 26753008]

(31). Plimpton S, Fast parallel algorithms for short-range molecular dynamics. J. Comput. Chem 1995, 117, 1–19.

(32). Rackers JA; Wang Z; Lu C; Laury ML; Lagardere L; Schnieders MJ; Piquemal JP; Ren P; Ponder JW, Tinker 8: Software Tools for Molecular Design. J. Chem. Theory Comput 2018, 14, 5273–5289. [PubMed: 30176213]

(33). Bowers KJ; Chow DE; Xu H; Dror RO; Eastwood MP; Gregersen BA; Klepeis JL; Kolossvary I; Moraes MA; Sacerdoti FD In Scalable algorithms for molecular dynamics simulations on commodity clusters, SC'06: Proceedings of the 2006 ACM/IEEE Conference on Supercomputing, IEEE: 2006; pp 43–43.

(34). Eastman P; Swails J; Chodera JD; McGibbon RT; Zhao Y; Beauchamp KA; Wang LP; Simmonett AC; Harrigan MP; Stern CD; Wiewiora RP; Brooks BR; Pande VS, OpenMM 7: Rapid development of high performance algorithms for molecular dynamics. PLoS Comp. Biol 2017, 13, e1005659.

(35). Klauda JB; Venable RM; Freites JA; O'Connor JW; Tobias DJ; Mondragon-Ramirez C; Vorobyov I; MacKerell AD Jr.; Pastor RW, Update of the CHARMM all-atom additive force field for lipids: validation on six lipid types. J. Phys. Chem. B 2010, 114, 7830–43. [PubMed: 20496934]

(36). Huang J; Rauscher S; Nawrocki G; Ran T; Feig M; de Groot BL; Grubmuller H; MacKerell AD Jr., CHARMM36m: an improved force field for folded and intrinsically disordered proteins. Nat. Methods 2017, 14, 71–73. [PubMed: 27819658]

(37). Interface Force Field (IFF) and a Surface Model Database https://bionanostructures.com/interface-md/. 2013–2021.

(38). Heinz H; Vaia RA; Farmer BL; Naik RR, Accurate Simulation of Surfaces and Interfaces of Face-Centered Cubic Metals Using 12−6 and 9−6 Lennard-Jones Potentials. J. Phys. Chem. C 2008, 112, 17281–17290.

(39). Kanhaiya K; Kim S; Im W; Heinz H, Accurate simulation of surfaces and interfaces of ten FCC metals and steel using Lennard–Jones potentials. npj Comput. Mater 2021, 7.

(40). Heinz H, Clay minerals for nanocomposites and biotechnology: surface modification, dynamics and responses to stimuli. Clay Miner 2018, 47, 205–230.

(41). Mishra RK; Flatt RJ; Heinz H, Force Field for Tricalcium Silicate and Insight into Nanoscale Properties: Cleavage, Initial Hydration, and Adsorption of Organic Molecules. J. Phys. Chem. C 2013, 117, 10417–10432.

(42). Mishra RK; Fernandez-Carrasco L; Flatt RJ; Heinz H, A force field for tricalcium aluminate to characterize surface properties, initial hydration, and organically modified interfaces in atomic resolution. Dalton Trans 2014, 43, 10602–16. [PubMed: 24828263]

(43). Emami FS; Puddu V; Berry RJ; Varshney V; Patwardhan SV; Perry CC; Heinz H, Force Field and a Surface Model Database for Silica to Simulate Interfacial Properties in Atomic Resolution. Chem. Mater 2014, 26, 2647–2658.

(44). Lin T-J; Heinz H, Accurate Force Field Parameters and pH Resolved Surface Models for Hydroxyapatite to Understand Structure, Mechanics, Hydration, and Biological Interfaces. J. Phys. Chem. C 2016, 120, 4975–4992.

(45). Pramanik C; Gissinger JR; Kumar S; Heinz H, Carbon Nanotube Dispersion in Solvents and Polymer Solutions: Mechanisms, Assembly, and Preferences. ACS Nano 2017, 11, 12805–12816. [PubMed: 29179536]

(46). Wang J; Wolf RM; Caldwell JW; Kollman PA; Case DA, Development and testing of a general amber force field. J. Comput. Chem 2004, 25, 1157–1174. [PubMed: 15116359]

(47). Best RB; Zhu X; Shim J; Lopes PE; Mittal J; Feig M; MacKerell AD Jr, Optimization of the additive CHARMM all-atom protein force field targeting improved sampling of the backbone ϕ, ψ and side-chain χ^1 and χ^2 dihedral angles. J. Chem. Theory Comput 2012, 8, 3257–3273. [PubMed: 23341755]

(48). Klauda JB; Venable RM; Freites JA; O'Connor JW; Tobias DJ; Mondragon-Ramirez C; Vorobyov I; MacKerell AD Jr; Pastor RW, Update of the CHARMM all-atom additive force field for lipids: validation on six lipid types. J. Phys. Chem. B 2010, 114, 7830–7843. [PubMed: 20496934]

(49). Hart K; Foloppe N; Baker CM; Denning EJ; Nilsson L; MacKerell AD Jr, Optimization of the CHARMM additive force field for DNA: Improved treatment of the BI/BII conformational equilibrium. J. Chem. Theory Comput 2012, 8, 348–362. [PubMed: 22368531]

(50). Schmid N; Eichenberger AP; Choutko A; Riniker S; Winger M; Mark AE; van Gunsteren WF, Definition and testing of the GROMOS force-field versions 54A7 and 54B7. Eur. Biophys. J 2011, 40, 843–856. [PubMed: 21533652]

(51). Kaminski GA; Friesner RA; Tirado-Rives J; Jorgensen WL, Evaluation and reparametrization of the OPLS-AA force field for proteins via comparison with accurate quantum chemical calculations on peptides. J. Phys. Chem. B 2001, 105, 6474–6487.

(52). Hirschfelder JO; Curtiss CF; Bird RB, Molecular theory of gases and liquids. Molecular theory of gases and liquids 1964.

(53). Heinz H; Castelijns HJ; Suter UW, Structure and phase transitions of alkyl chains on mica. Journal of the American Chemical Society 2003, 125, 9500–9510. [PubMed: 12889981]

(54). Steinbach PJ; Brooks BR, New spherical-cutoff methods for long-range forces in macromolecular simulation. J. Comput. Chem 1994, 15, 667–683.

(55). Shirts MR; Klein C; Swails JM; Yin J; Gilson MK; Mobley DL; Case DA; Zhong ED, Lessons learned from comparing molecular dynamics engines on the SAMPL5 dataset. J. Comput.-Aided Mol. Des 2017, 31, 147–161. [PubMed: 27787702]

(56). Lide DR, CRC handbook of chemistry and physics 84th ed.; CRC press: Boca Raton, 2004; Vol. 85.

(57). Schönfeld B; Huang JJ; Moss SC, Anisotropic mean-square displacements (MSD) in single-crystals of 2H- and 3R-MoS2. Acta Crystallogr. Sect. B: Struct. Sci 1983, 39, 404–407.

(58). Heaney PJ; Prewitt CT; Gibbs GV, Silica: Physical behavior, geochemistry, and materials applications Walter de Gruyter GmbH & Co KG: 2018; Vol. 29.

(59). Tran R; Xu Z; Radhakrishnan B; Winston D; Sun W; Persson KA; Ong SP, Surface energies of elemental crystals. Sci. Data 2016, 3, 1–13.

(60). Choi YK; Park SJ; Park S; Kim S; Kern NR; Lee J; Im W, CHARMM-GUI Polymer Builder for Modeling and Simulation of Synthetic Polymers. J. Chem. Theory Comput 2021, 17, 2431–2443. [PubMed: 33797913]

(61). Essmann U; Perera L; Berkowitz ML; Darden T; Lee H; Pedersen LG, A smooth particle mesh Ewald method. J. Chem. Phys 1995, 103, 8577–8593.

(62). Ryckaert J-P; Ciccotti G; Berendsen HJC, Numerical integration of the cartesian equations of motion of a system with constraints: molecular dynamics of n-alkanes. J. Comput. Phys 1977, 23, 327–341.

(63). Hess B; Bekker H; Berendsen HJ; Fraaije JG, LINCS: a linear constraint solver for molecular simulations. J. Comput. Chem 1997, 18, 1463–1472.

(64). Lee J; Hitzenberger M; Rieger M; Kern NR; Zacharias M; Im W, CHARMM-GUI supports the Amber force fields. J. Chem. Phys 2020, 153, 035103. [PubMed: 32716185]

(65). Wulff G, XXV. Zur Frage der Geschwindigkeit des Wachsthums und der Auflösung der Krystallflächen. Z. Kristallogr. Cryst. Mater 1901, 34, 449–530.

(66). Murray HH, Overview — clay mineral applications. Appl. Clay Sci 1991, 5, 379–395.

(67). Massaro M; Colletti CG; Lazzara G; Riela S, The Use of Some Clay Minerals as Natural Resources for Drug Carrier Applications. J. Funct. Biomater 2018, 9.

(68). Teich-McGoldrick SL; Greathouse JA; Cygan RT, Molecular dynamics simulations of structural and mechanical properties of muscovite: pressure and temperature effects. The Journal of Physical Chemistry C 2012, 116, 15099–15107.

(69). Teich-McGoldrick SL; Greathouse JA; Cygan RT, Molecular Dynamics Simulations of Structural and Mechanical Properties of Muscovite: Pressure and Temperature Effects. J. Phys. Chem. C 2012, 116, 15099–15107.

(70). Hoffmann F; Cornelius M; Morell J; Froba M, Silica-based mesoporous organic-inorganic hybrid materials. Angew. Chem. Int. Ed. Engl 2006, 45, 3216–51. [PubMed: 16676373]

(71). Slowing II; Trewyn BG; Giri S; Lin VSY, Mesoporous Silica Nanoparticles for Drug Delivery and Biosensing Applications. Adv. Funct. Mater 2007, 17, 1225–1236.

(72). Hassanali AA; Zhang H; Knight C; Shin YK; Singer SJ, The Dissociated Amorphous Silica Surface: Model Development and Evaluation. J. Chem. Theory Comput 2010, 6, 3456–71. [PubMed: 26617097]

(73). Lopes PE; Murashov V; Tazi M; Demchuk E; Mackerell AD Jr., Development of an empirical force field for silica. Application to the quartz-water interface. J. Phys. Chem. B 2006, 110, 2782–92. [PubMed: 16471886]

(74). Goumans TP; Wander A; Brown WA; Catlow CR, Structure and stability of the (001) alpha-quartz surface. Phys. Chem. Chem. Phys 2007, 9, 2146–52. [PubMed: 17464397]

(75). Lamb RN; Furlong DN, Controlled wettability of quartz surfaces. J. Chem. Soc., Faraday Trans 1 1982, 78.

(76). Gajjeraman S; Narayanan K; Hao J; Qin C; George A, Matrix macromolecules in hard tissues control the nucleation and hierarchical assembly of hydroxyapatite. J. Biol. Chem 2007, 282, 1193–204. [PubMed: 17052984]

(77). Liao C; Xie Y; Zhou J, Computer simulations of fibronectin adsorption on hydroxyapatite surfaces. RSC Advances 2014, 4, 15759–15769.

(78). Schneider C; Glazov MM; Korn T; Hofling S; Urbaszek B, Two-dimensional semiconductors in the regime of strong light-matter coupling. Nat. Commun 2018, 9, 2695. [PubMed: 30002368]

(79). Wen M; Shirodkar SN; Plecháč P; Kaxiras E; Elliott RS; Tadmor EB, A force-matching Stillinger-Weber potential for MoS2: Parameterization and Fisher information theory based sensitivity analysis. J. Appl. Phys 2017, 122.

(80). Jo S; Cheng X; Islam SM; Huang L; Rui H; Zhu A; Lee HS; Qi Y; Han W; Vanommeslaeghe K; MacKerell AD Jr.; Roux B; Im W, CHARMM-GUI PDB manipulator for advanced modeling and simulations of proteins containing nonstandard residues. Adv. Protein Chem. Struct. Biol 2014, 96, 235–65. [PubMed: 25443960]

(81). Ramezani-Dakhel H; Ruan L; Huang Y; Heinz H, Molecular Mechanism of Specific Recognition of Cubic Pt Nanocrystals by Peptides and of the Concentration-Dependent Formation from Seed Crystals. Adv. Funct. Mater 2015, 25, 1374–1384.

(82). Main AL; Harvey TS; Baron M; Boyd J; Campbell ID, The three-dimensional structure of the tenth type III module of fibronectin: An insight into RGD-mediated interactions. Cell 1992, 71, 671–678. [PubMed: 1423622]

(83). Petrie TA; Reyes CD; Burns KL; Garcia AJ, Simple application of fibronectin-mimetic coating enhances osseointegration of titanium implants. J. Cell. Mol. Med 2009, 13, 2602–2612. [PubMed: 18752639]

(84). Richter RP; Bérat R; Brisson AR, Formation of solid-supported lipid bilayers: an integrated view. Langmuir 2006, 22, 3497–3505. [PubMed: 16584220]

(85). Chun MJ; Choi YK; Ahn DJ, Formation of nanopores in DiynePC–DPPC complex lipid bilayers triggered by on-demand photo-polymerization. RSC Advances 2018, 8, 27988–27994.

(86). Richter RP; Brisson AR, Following the formation of supported lipid bilayers on mica: a study combining AFM, QCM-D, and ellipsometry. Biophys. J 2005, 88, 3422–3433. [PubMed: 15731391]

(87). Wu EL; Cheng X; Jo S; Rui H; Song KC; Davila-Contreras EM; Qi Y; Lee J; Monje-Galvan V; Venable RM; Klauda JB; Im W, CHARMM-GUI Membrane Builder toward realistic biological membrane simulations. J. Comput. Chem 2014, 35, 1997–2004. [PubMed: 25130509]

(88). Jo S; Lim JB; Klauda JB; Im W, CHARMM-GUI Membrane Builder for mixed bilayers and its application to yeast membranes. Biophys. J 2009, 97, 50–8. [PubMed: 19580743]

(89). Jo S; Kim T; Im W, Automated builder and database of protein/membrane complexes for molecular dynamics simulations. PLoS One 2007, 2, e880. [PubMed: 17849009]

(90). Tadmor EB; Elliott RS; Sethna JP; Miller RE; Becker CA, The potential of atomistic simulations and the knowledgebase of interatomic models. JOM 2011, 63, 17–17.

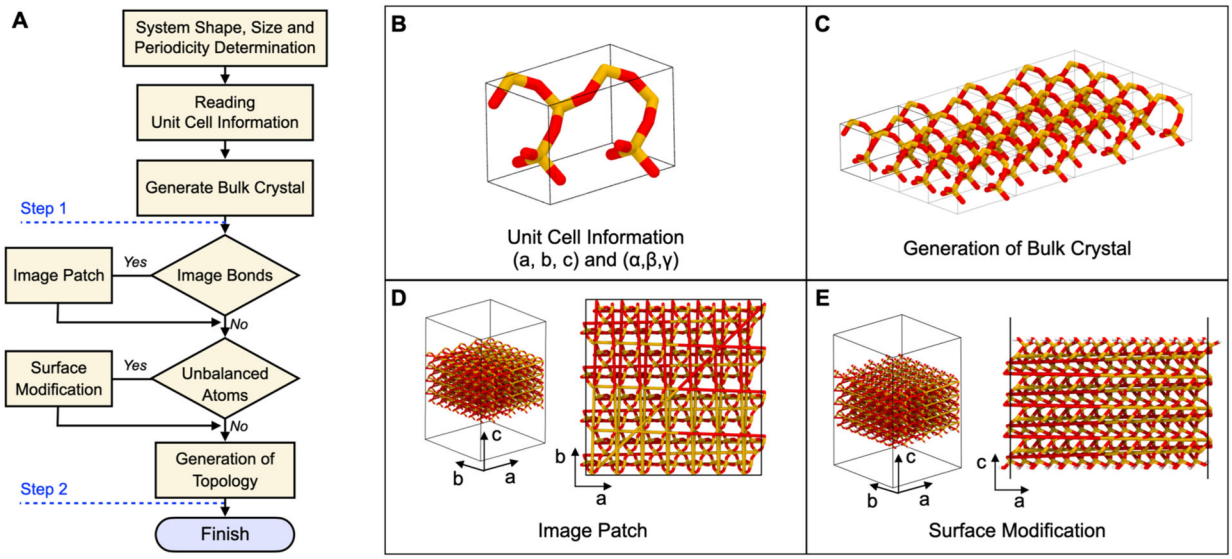

Figure 1.

Illustration of the *Nanomaterial Modeler* workflow. (A) Workflow of *Nanomaterial Modeler*. (B) Unit cell information is used to build nanomaterials. (C) Each unit cell structure is duplicated and translated for the generation of user-specified system size. (D) For systems having bonds along a specific direction, bond linkages across the neighboring periodic images are built. (E) Surface modification is performed to facilitate hydrogenation and ionization.

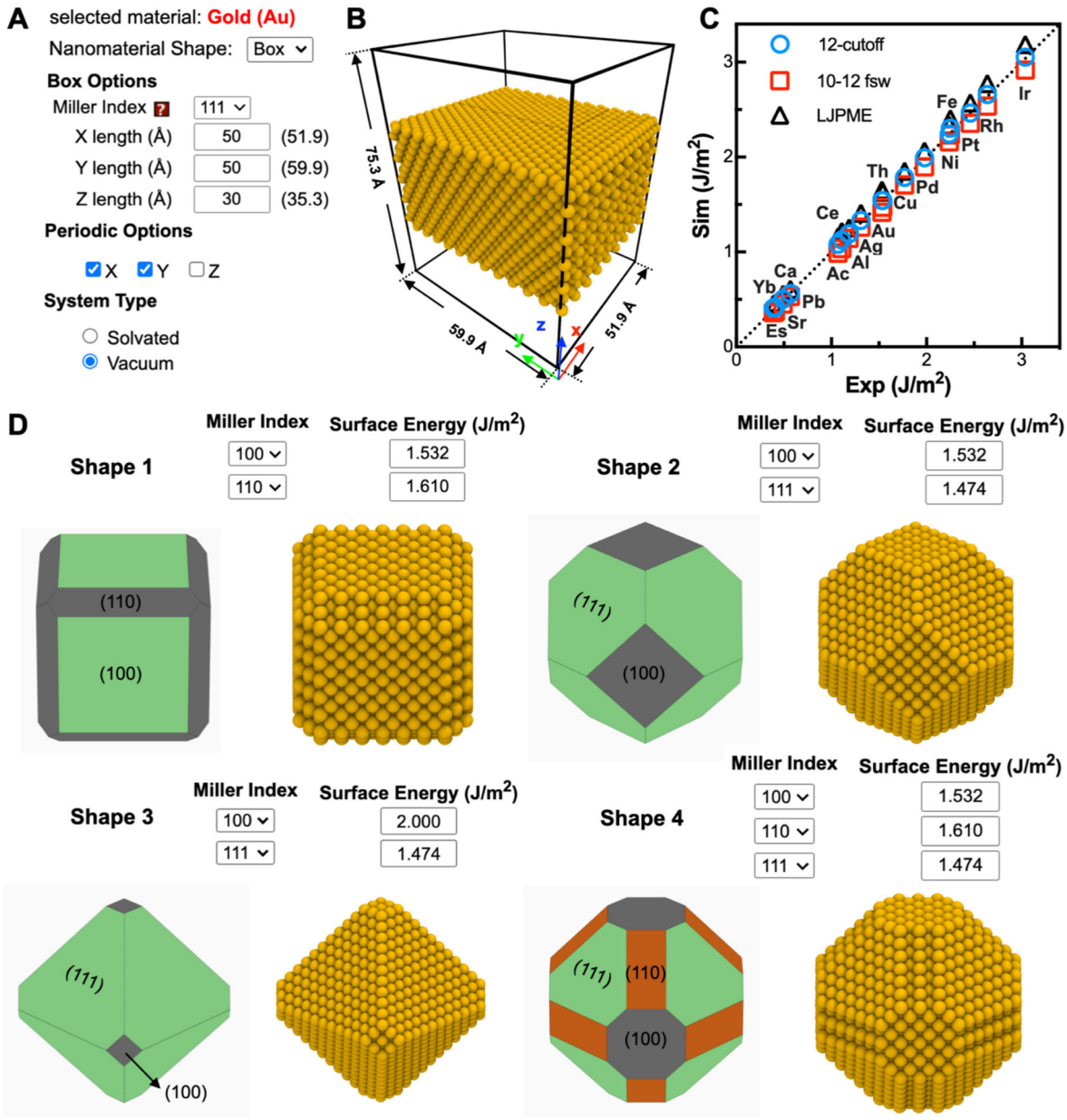

Figure 2.

Building surfaces and equilibrium shapes of gold nanoparticles using *Nanomaterial Modeler*. (A) User interface of *Nanomaterial Modeler* for building a (111) gold surface. One can select X, Y, and Z under "Periodic Options" to define the periodicity of the gold surface along each axis and choose a "System Type" to build the nanomaterial in water or in vacuum. (B) All-atom model obtained from the options in (A). (C) Comparison of simulated and experimental surface energies of 18 fcc metals for (111) surfaces. Three LJ cut-off methods (i.e., 12 Å cut-off, 10–12 Å fsw, and LJPME) were used to calculate surface energies. (D) Predicted equilibrium shapes using Wulff construction and corresponding all-atom models of gold nanoparticles. The shape depends on a combination of Miller indices and the corresponding surface energies.

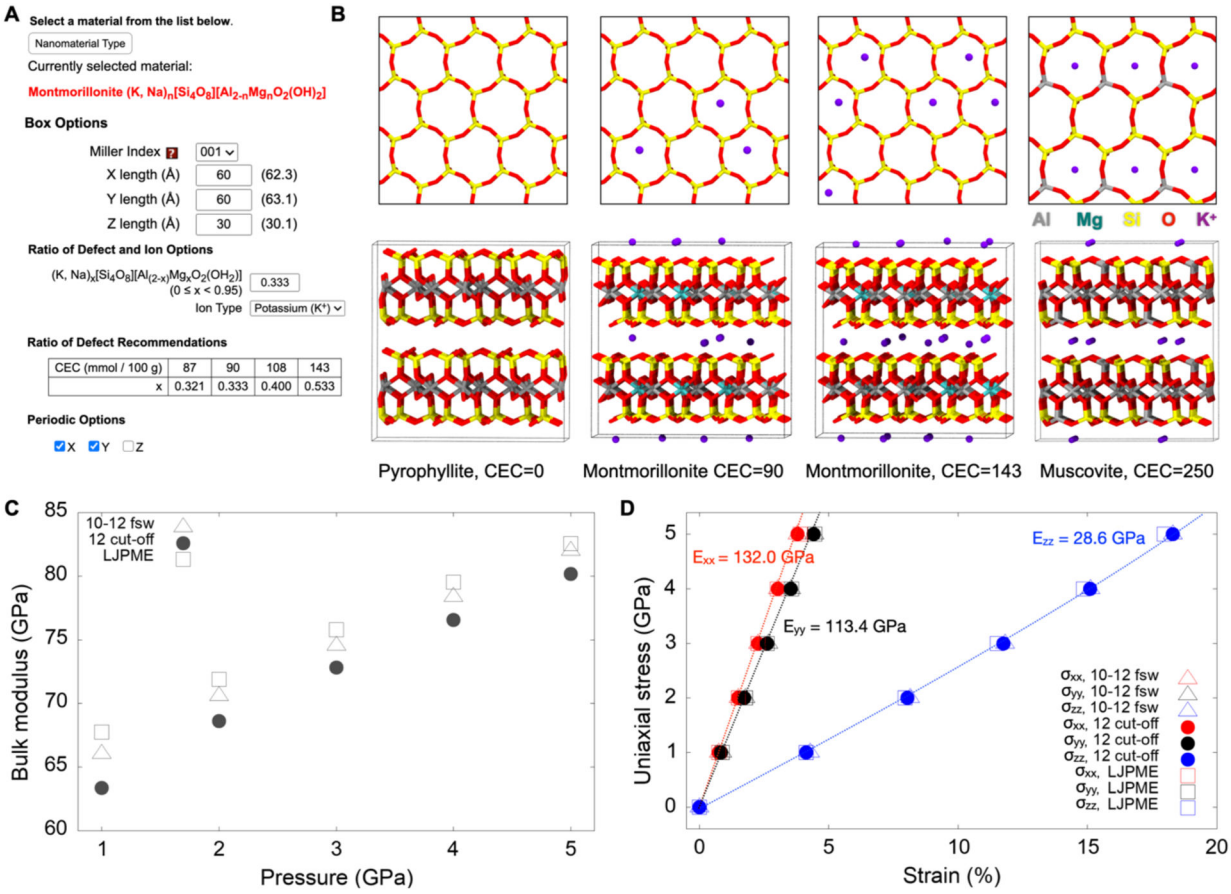

Figure 3.

(A) User interface to generate 0.333 mmol/100g cation exchange capacity (CEC) montmorillonite. (B) Illustrative snapshots of top (upper panel) and side (lower panel) views of pyrophyllite, montmorillonite, and muscovite. In the top view, the layers located below the top layer are hidden to show the different CEC states clearly. (C) The bulk modulus of muscovite with different LJ cut-off methods as a function of applied pressure. (D) Young's modulus of muscovite along the X, Y, and Z direction with different LJ methods. Error bars are smaller than the symbol size. Aluminum, magnesium, silicon, oxygen, and potassium ion are colored in gray, green, yellow, red, and purple, respectively.

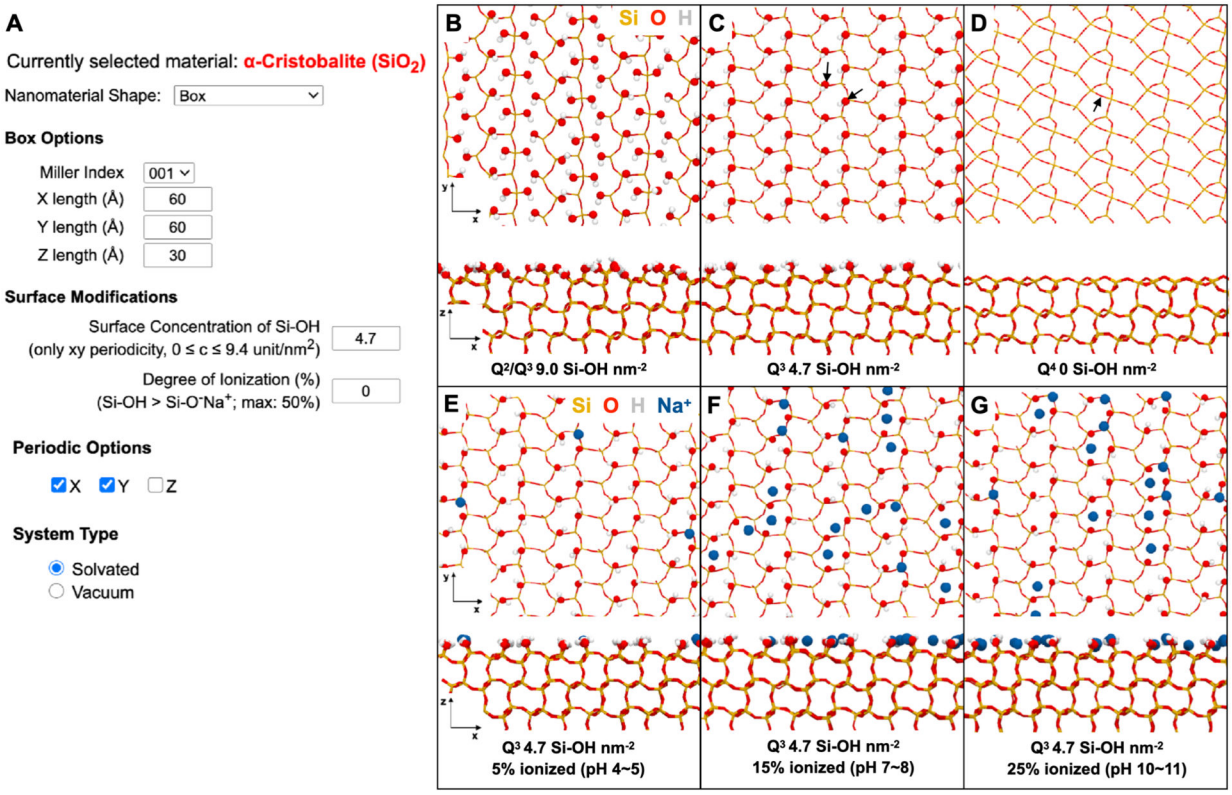

Figure 4.

Generation of silica surface models using *Nanomaterial Modeler*. (A) User interface to build a (20-2) α-cristobalite surface with a size of 60 × 60 × 30 $Å^3$. (B-D) Q^2/Q^3, Q^3, and Q^4 surfaces with a total Si-OH density of 9.0 nm^{-2}, 4.7 nm^{-2}, and 0 nm^{-2} with top (upper panel) and side views (lower panel). Black arrows indicate the formation of siloxide bridges from two silanol groups. (E-G) Q^3 surfaces with a total Si-O(H, Na) density of 4.7 nm^{-2} and 5%, 15%, and 25% ionization with top (upper panel) and side (lower panel) views. Silica, oxygen, hydrogen, and sodium are colored in yellow, red, gray, and blue.

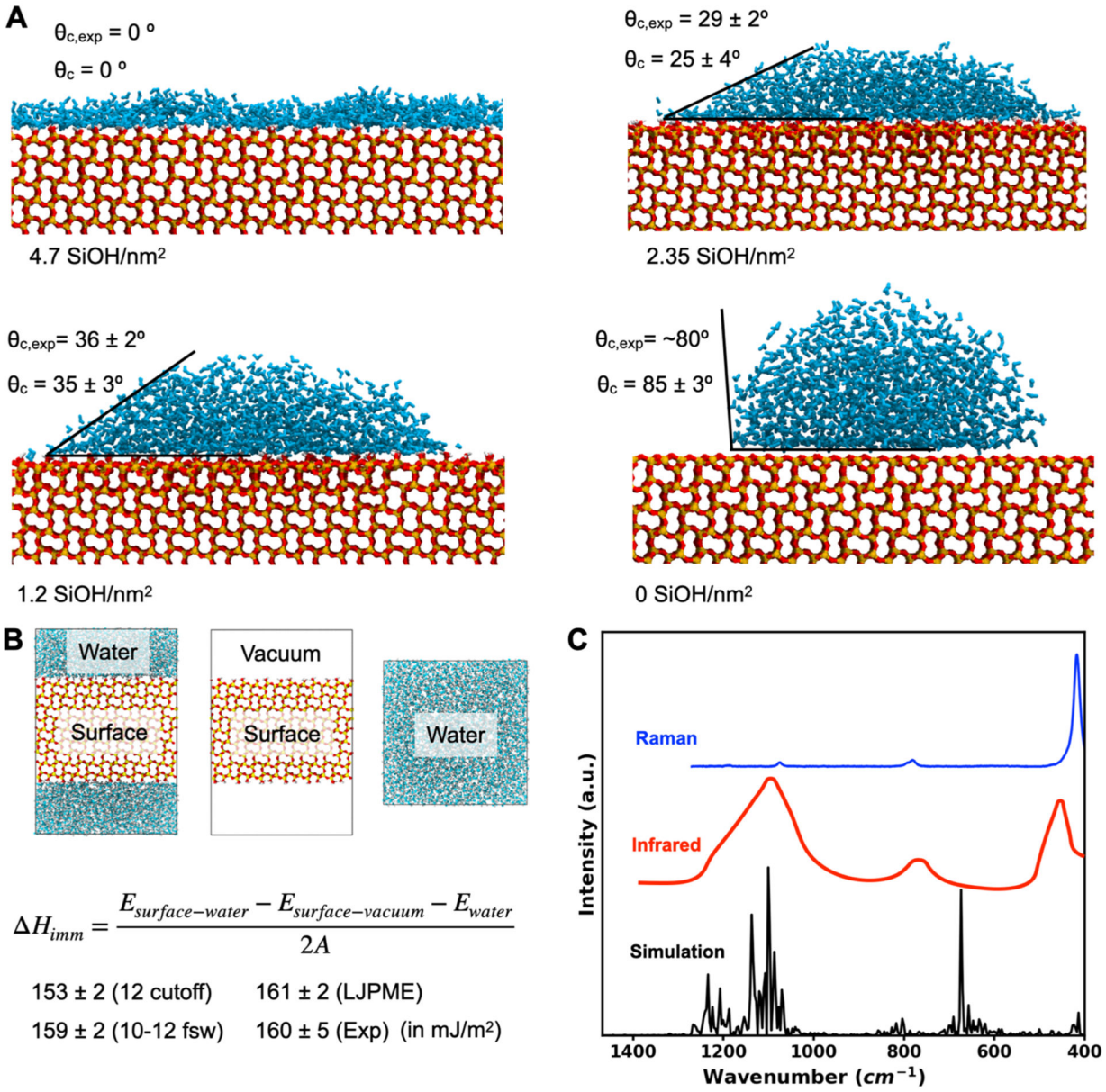

Figure 5.

Silica-water interfacial properties and vibrational spectrum. (A) Water contact angles on silica surfaces ranging from Q^3 to Q^4 environments. Experimental results are obtained from ref[75]. (B) The heat of immersion of silica surfaces in water. Three systems were generated to compute $E_{surface-water}$, $E_{surface-vacuum}$, and E_{water}, respectively (upper panel). Results of Q^3 surfaces using different LJ cut-off methods and experiments (lower panel) are shown. (C) Vibration spectrum of α-cristobalite from the simulation in comparison with experimental infrared and Raman spectra.

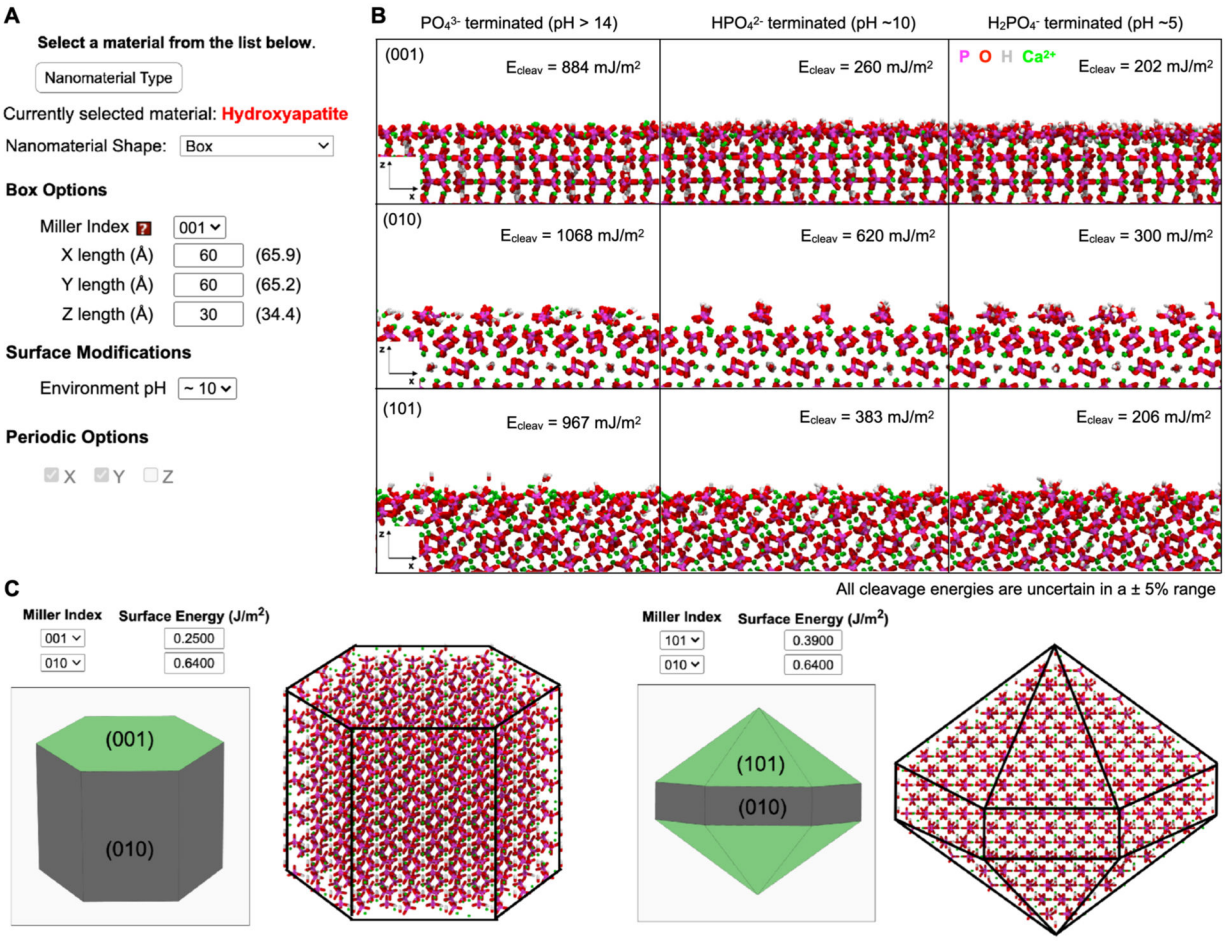

Figure 6.

Generation of hydroxyapatite (HAP) surfaces and nanocrystals. (A) User interface for the generation of HAP surfaces. *Nanomaterial Modeler* supports (001), (010), (020), and (101) surface with three hydrogenation states based on strong basic (pH > 14), basic (pH ~10), and mildly acidic (pH ~5) conditions. (B) Illustrative snapshots of relaxed surface models of HAP and calculated cleavage energies in vacuum in different pH environments. (C) Predicted and corresponding all-atom models of rod-like (left) and elongated hexagonal bipyramid (right) shapes of HAP nanocrystals. Phosphate, oxygen, hydrogen, and calcium ion are colored in magenta, red, white, and green, respectively.

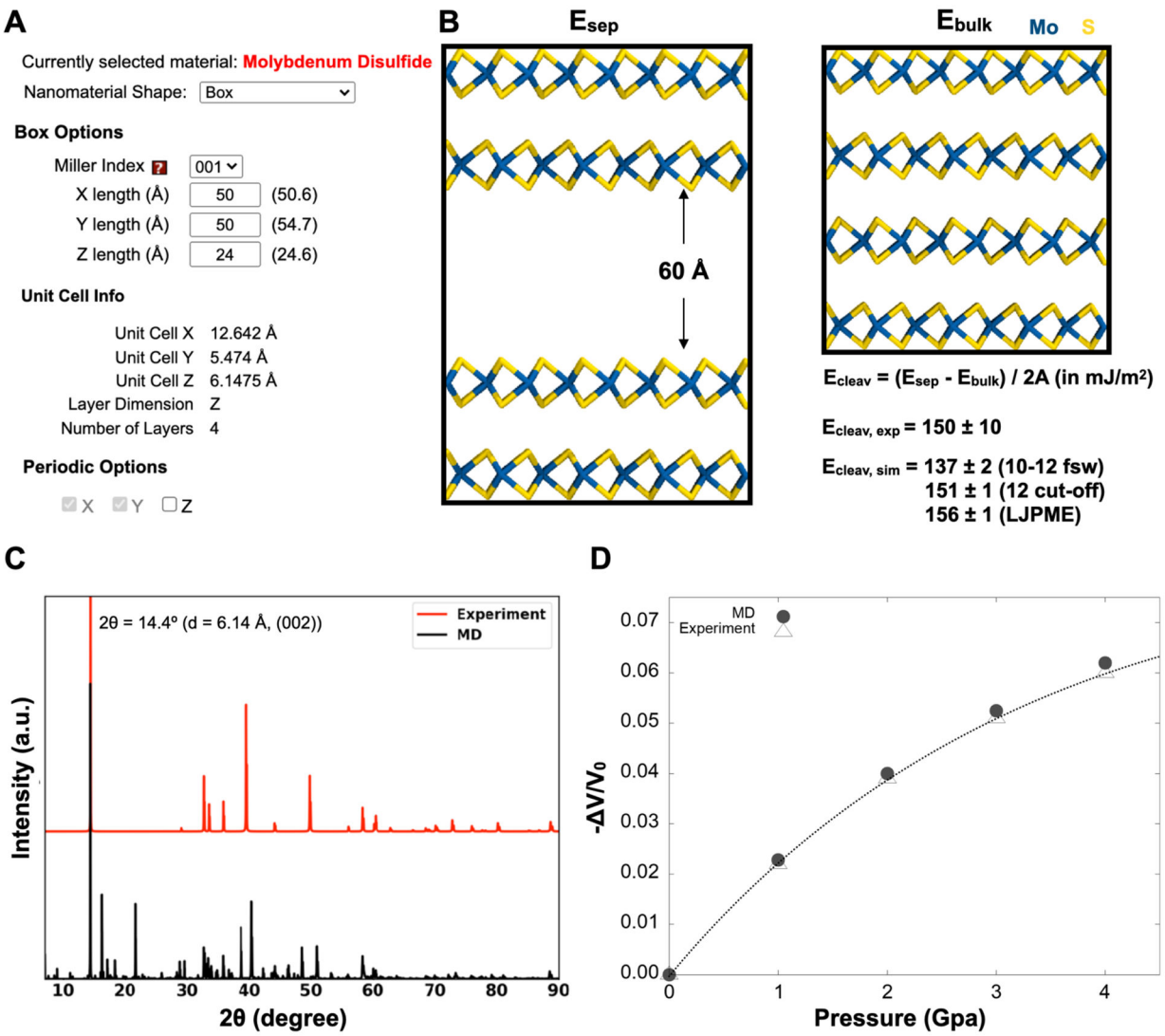

Figure 7.

(A) User interface for building 2H-MoS_2 layers. (B) The models used to calculate the cleavage energy comprise a cleaved surface slab of four MoS_2 layers with a 60 Å vacuum layer (left) and the equivalent periodic bulk systems (right). E_{sep} and E_{bulk} represent the potential energy of separated and bulk systems, respectively. A is the surface area. (C) X-ray powder diffraction (XRD) pattern comparison between the experimental data[57] (red) and the MD result (black). (D) The compressibility of bulk MoS_2 from experiment and simulation.

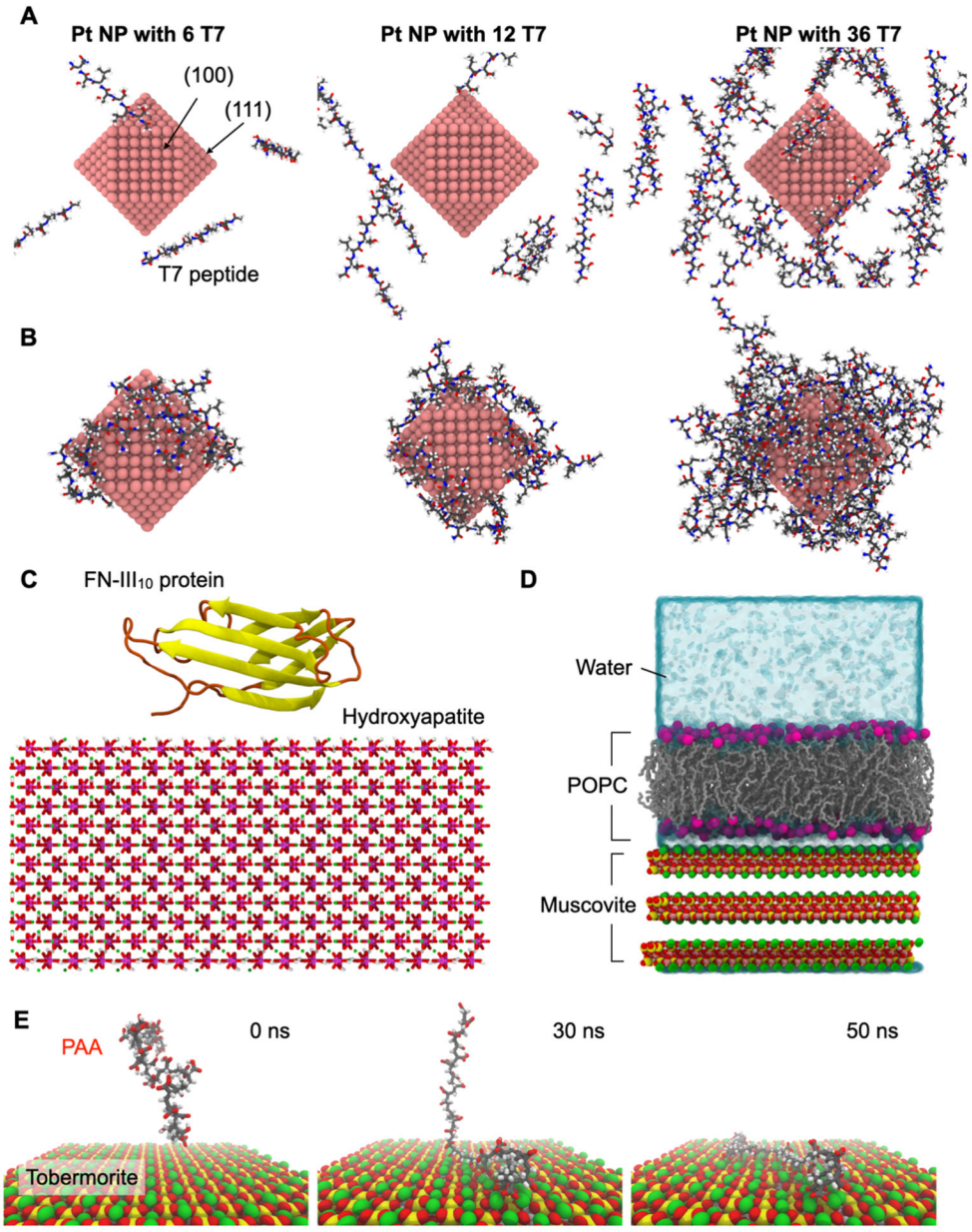

Figure 8.

Illustrative snapshots of (A) initial and (B) final simulation systems for a platinum (Pt) nanoparticle with T7 peptides. Pt, nitrogen, carbon, oxygen, and hydrogen atoms are colored in pink, blue, gray, red, and white. (C) hydroxyapatite surface with FN-III10 protein. Hydroxyapatite is colored as in Figure 4. FN-III10 proteins are represented in a cartoon with different colors based on the secondary structures (yellow for β-sheet and orange for coil and turn). (D) Supported lipid bilayer composed of 1-palmitoyl-2-oleoyl-*sn*-phophatidylcholine (POPC) and muscovite. Phosphorus, carbon, silica, oxygen, hydrogen, calcium, and aluminum atoms are colored in magenta, gray, yellow, red, white, green, and pink, respectively. (E) Snapshots of poly(acrylic acid) adsorption on a tobermorite (004)

facet. The color code is the same as (D). Water molecules are omitted for clarity except for (D).

Table 1.

Nanomaterials available in *Nanomaterial Modeler* and corresponding references.

Class	Material (Chemical formula)	Shape	Remarks
Fcc metals	Ac, Ag, Al, Au, Ca, Ce, Cu, Es, Fe, Ir, Ni, Pb, Pd, Pt, Rh, Sr, Th, and Yb	box[a], cylinder, rod, polygon, sphere, Wulff	ref[38,39]
Clay Minerals	Pyrophyllite ($Al_2Si_4O_{10}(OH)_2$)	box	ref[40]
	Kaolinite ($Al_2Si_2O_5(OH)_4$)	box	ref[40]
	Montmorillonite ($(K, Na)_n[Si_4O_8][Al_{2-n}Mg_nO_2(OH)_2]$)	box	ref[40]
	Muscovite ($KAl_2(AlSi_3)O_{10}(OH)_2$)	box	ref[40]
Calcium Sulfates	Gypsum ($CaSO_4{\cdot}2H_2O$)	box, Wulff	ref[13]
	Hemihydrate ($CaSO_4{\cdot}1/2H_2O$)	box	ref[13]
	Anhydrite ($CaSO_4$)	box	ref[13]
Cement Minerals	Tricalcium Silicate (Ca_3SiO_5)	box, Wulff	ref[41]
	Tricalcium Aluminate ($Ca_3Al_2O_6$)	box	ref[42]
Calcium Silicate Hydrate	Tobermorite ($Ca_4Si_6O_{15}(OH)_2{\cdot}5H_2O$)	box	ref[42]
Silica	α-quartz (SiO_2)	box, sphere	ref[43]
	α-cristobalite (SiO_2)	box, sphere	ref[43]
Phosphate Minerals	Hydroxyapatite ($Ca_5(PO_4)_3(OH)$)	box, Wulff	ref[44]
Transition Metal Dichalcogenides	Molybdenum (MoS_2)	box	ref[15]
Carbonaceous Materials	Carbon Nanotube	-	ref[45]
	Graphene	box, hexagonal	ref[45]
	Graphite	box	ref[45]

[a]Box represents a rectangular parallelepiped shape.